SCLM origin of these peridotites is the close spatial proximity of mantle with such widely varying extraction ages, when every other geochemical aspect of the peridotites suggests they are petrogenetically related (*9, 10*).

These Os isotope data indicate that unusually old depleted mantle is stranded within subduction zones. Our preferred interpretation is that the peridotites analyzed are from the oceanic mantle, which suggests that portions of the upper mantle are less radiogenic in Os isotopes than previously recognized.

References and Notes

1. M. I. Smoliar, R. J. Walker, J. W. Morgan, *Science* **271**, 1099 (1996).
2. D. G. Pearson, R. W. Carlson, S. B. Shirey, F. R. Boyd, P. H. Nixon, *Earth Planet. Sci. Lett.* **134**, 341 (1995); D. G. Pearson *et al.*, *Geochim. Cosmochim. Acta* **59**, 959 (1995).
3. L. Reisberg and J.-P. Lorand, *Nature* **376**, 159 (1995).
4. M. R. Handler, V. C. Bennett, T. M. Esat, *Earth Planet. Sci. Lett.* **151**, 61 (1997).
5. M. Roy-Barman and C. J. Allègre, *Geochim. Cosmochim. Acta* **58**, 5043 (1994); J. E. Snow and L. Reisberg, *Earth Planet. Sci. Lett.* **133**, 411 (1995).
6. A. D. Brandon, R. A. Creaser, S. B. Shirey, R. W. Carlson, *Science* **272**, 861 (1996).
7. P. Fryer, E. L. Ambos, D. M. Hussong, *Geology* **13**, 774 (1985); P. Fryer, *Proc. ODP Sci. Res.* **125**, 593 (1992).
8. J. A. Pearce *et al.*, *Proc. ODP Sci. Res.* **125**, 623 (1992); B. Taylor, *ibid.* **126**, 627 (1992).
9. I. J. Parkinson, J. A. Pearce, M. F. Thirlwall, K. T. M. Johnson, G. Ingram, *ibid.* **125**, 487 (1992).
10. I. J. Parkinson and J. A. Pearce, *J. Petrol.* **39**, 1577 (1998).
11. The surfaces of the rock samples were cleaned to remove any obvious alteration material. The samples were then milled in an agate Tema until a very fine powder was produced. Powder (2 g) was spiked and digested with aqua regia in a Carius tube. Os and Re were separated using a solvent extraction scheme and were purified using a microdistillation method and small anion columns, respectively. Os concentrations, $^{187}Os/^{188}Os$ ratios, and Re concentrations were measured as negative ions on a Finnigan 261 mass spectrometer. Analytical methods are presented in detail elsewhere [A. S. Cohen and F. G. Waters, *Anal. Chim. Acta* **332**, 269 (1996)]. Precision of the $^{187}Os/^{188}Os$ ratios, based on counting statistics, ranges from 0.03 to 0.13% (2σ). Standards run during the course of this work are reproduced at a precision of 0.2%. A full procedural replicate analysis of one sample agreed within 0.15%. Unfortunately, there was a considerable difference in the Os concentration between the replicates, suggesting some heterogeneity in distribution of Os in the sample. However, the fact that the replicates have identical $^{187}Os/^{188}Os$ ratios supports the notion that there is negligible Re in the peridotites. Procedural blanks for Os during the course of this work varied from 16 pg to less than 2 pg. Blank corrections ranged from 0.02 to 1.5%. Re concentrations were negligible ($<$10 ppt) and were swamped by the Re blank.
12. REE data from (*10*); the amphibole-bearing harzburgite has a smooth REE pattern increasing from La to Lu. By contrast, all the other samples have U-shaped patterns with variable light REE enrichment.
13. Seawater alteration and sea-floor weathering processes both add radiogenic Os to peridotites (*5*). Drilled peridotites that have not weathered on the sea floor are generally not affected by Os addition (*5*). Roy-Barman and Allègre leached an ODP-drilled peridotite with oxalic acid and found no difference in the $^{187}Os/^{188}Os$ ratio of the unleached and leached sample. The peridotites in this study are serpentinized but are all from deep sections of the drill core. No manganoan coating was observed on the peridotites. Moreover, it has been suggested that serpentinization of these peridotites is not by seawater alteration at a ridge crest, but by fluids from the underlying subducting plate [M. J. Mottl, *Proc. ODP Sci. Res.* **125**, 373 (1992)].
14. D. R. Hassler and N. Shimizu, *Science* **280**, 418 (1998).
15. Al_2O_3 data from (*10*).
16. In the model age calculation, the peridotite is assumed to contain no Re, and therefore the $^{187}Os/^{188}Os$ ratio of the peridotite has not changed because the Re was extracted during an ancient melting event. The age is calculated from the time in the past that the measured $^{187}Os/^{188}Os$ ratio intersects a chondritic Re-Os evolution curve with a present-day $^{187}Os/^{188}Os$ ratio of 0.12757 and a $^{187}Re/^{188}Os$ ratio of 0.3972 [R. J. Walker, R. W. Carlson, S. B. Shirey, F. R. Boyd, *Geochim. Cosmochim. Acta* **53**, 1583 (1989)]. Recent work suggests that the putative primitive upper mantle has an $^{187}Os/^{188}Os$ ratio of 0.1290 and a $^{187}Re/^{188}Os$ ratio of 0.423 [T. Meisel, R. J. Walker, J. W. Morgan, *Nature* **383**, 517 (1996)]. Using these parameters gives slightly older (100 Ma) model ages but does not affect our conclusions.
17. T_{RD} model ages from DMM are calculated in a similar fashion to (*16*) except that the $^{187}Os/^{188}Os$ ratio of modern-day DMM is taken to be 0.1246 (*5*) and that it is extracted from a chondritic mantle at 2500 Ma. This calculation depends on the age of extraction of the DMM reservoir from the primitive mantle, but T_{RD} from DMM always gives a younger model age than does T_{RD} from the chondritic mantle.
18. The refectory nature of the Leg 125 peridotites (highly forsteritic olivine, low Al_2O_3 contents) means that its density is still slightly lower than that of ambient fertile mantle, even when the peridotites have cooled substantially. Therefore, it is relatively buoyant and will become stabilized (see W. L. Griffin, S. Y. O'Reilly, C. G. Ryan, O. Gaul, D. A. Ionov, *AGU Spec. Monogr.*, in press).
19. Modeling of the amount of melt extraction is as follows: For each peridotite, an initial Re content is assigned using its Os content and the assumption that it has a chondritic Re/Os ratio of 0.8. The simplest approach is to assume that Os has a bulk partition value of 1, so the Os concentration does not change during melting. Using more realistic Os partition values does not markedly change the conclusion of the calculations. The Re concentration and therefore the $^{187}Re/^{188}Os$ ratio is changed such that the sample would evolve from the chondritic mantle curve (*15*) to its measured $^{187}Os/^{188}Os$ ratio for any given extraction date. The amount of melting is then calculated using the observation that Re and Al_2O_3 correlate linearly during partial melting and that Re is completely extracted after ~25% partial melting. Although modeling assumptions change the absolute values calculated, each calculation is internally consistent and the relative difference in partial melting between samples is also consistent.
20. A. Zindler and S. R. Hart, *Annu. Rev. Earth Planet. Sci.* **14**, 493 (1986).
21. M. T. McCulloch and V. C. Bennett, *Geochim. Cosmochim. Acta* **58**, 4717 (1994).
22. W. M. White, *Earth Planet. Sci. Lett.* **115**, 211 (1993).
23. γOs is a percentage difference between the measured $^{187}Os/^{188}Os$ ratio and the $^{187}Os/^{188}Os$ ratio of present-day mantle. In this case we use a present-day $^{187}Os/^{188}Os$ ratio of 0.12757 (*16*). Negative γOs values indicate subchondritic Os isotope rations; positive values indicate suprachondritic ratios.
24. L. Reisberg, C. J. Allègre, J. M. Luck, *Earth Planet. Sci. Lett.* **107**, 406 (1991); T. Meisel, R. J. Walker, J. W. Morgan, *Nature* **383**, 517 (1996); O. M. Burnham, N. W. Rogers, D. G. Pearson, P. W. van Calsteren, C. J. Hawkesworth, *Geochim. Cosmochim. Acta* **62**, 229 (1998).
25. P. J. Michael and E. Bonatti, *Init. Rep. Deep Sea Drill. Progr.* **82**, 523 (1985); J. E. Snow and H. J. B. Dick, *Geochim. Cosmochim. Acta* **59**, 4219 (1995).

26. We thank J. Bartlett for assistance in the laboratory. I.J.P. is funded by a Natural Environment Research Council (NERC)/ODP Fellowship, and isotope facilities at the Open University are supported by NERC.

10 July 1998; accepted 18 August 1998

Semiconductor Nanocrystals as Fluorescent Biological Labels

Marcel Bruchez Jr., Mario Moronne, Peter Gin, Shimon Weiss,* A. Paul Alivisatos*

Semiconductor nanocrystals were prepared for use as fluorescent probes in biological staining and diagnostics. Compared with conventional fluorophores, the nanocrystals have a narrow, tunable, symmetric emission spectrum and are photochemically stable. The advantages of the broad, continuous excitation spectrum were demonstrated in a dual-emission, single-excitation labeling experiment on mouse fibroblasts. These nanocrystal probes are thus complementary and in some cases may be superior to existing fluorophores.

Fluorescence is a widely used tool in biology. The drive to measure more biological indicators simultaneously imposes new demands on the fluorescent probes used in these experiments. For example, an eight-color, three-laser system has been used to measure a total of 10 parameters on cellular antigens with flow cytometry (*1*), and in cytogenetics, combinatorial labeling has been used to generate 24 falsely colored probes for spectral karyotyping (*2*). Conventional dye molecules impose stringent requirements on the optical systems used to make these measurements; their narrow excitation spectrum makes simultaneous excitation difficult in most cases, and their broad emission spectrum with a long tail at red wavelengths (Fig. 1A) introduces spectral cross talk between different detection channels, making quantita-

M. Bruchez Jr. and A. P. Alivisatos, Department of Chemistry, University of California, Berkeley, CA 94720, and Materials Sciences Division, Lawrence Berkeley National Laboratory (LBNL), 1 Cyclotron Road, Berkeley, CA 94720, USA. M. Moronne and P. Gin, Life Sciences Division, LBNL, 1 Cyclotron Road, Berkeley, CA 94720, USA. S. Weiss, Materials Sciences Division and Physical Biosciences Division. LBNL, 1 Cyclotron Road, Berkeley, CA 94720, USA.

*To whom correspondence should be addressed. E-mail: sweiss@mhl.lbl.gov and alivis@uclink4.berkeley.edu

tion of the relative amounts of different probes difficult. Ideal probes for multicolor experiments should emit at spectrally resolvable energies and have a narrow, symmetric emission spectrum, and the whole group of probes should be excitable at a single wavelength (*3, 4*).

In semiconductor nanocrystals, the absorbance onset and emission maximum shift to higher energy with decreasing size (*5*). The excitation tracks the absorbance, resulting in a tunable fluorophore that can be excited efficiently at any wavelength shorter than the emission peak yet will emit with the same characteristic narrow, symmetric spectrum regardless of the excitation wavelength (Fig. 1B). Variation of the material used for the nanocrystal and variation of the size of the nanocrystal afford a spectral range of 400 nm to 2 μm in the peak emission (Fig. 2), with typical emission widths of 20 to 30 nm [full width at half maximum (FWHM)] in the visible region of the spectrum and large extinction coefficients in the visible and ultraviolet range ($\sim 10^5\ M^{-1}\ cm^{-1}$). Many sizes of nanocrystals may therefore be excited with a single wavelength of light, resulting in many emission colors that may be detected simultaneously.

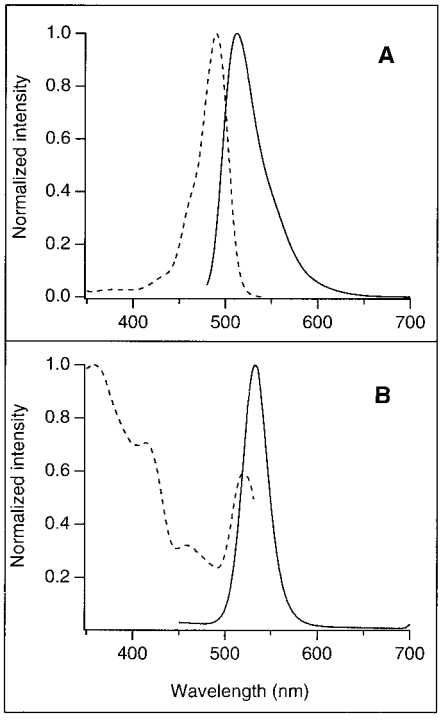

Fig. 1. Excitation (dashed) and fluorescence (solid) spectra of (**A**) fluorescein and (**B**) a typical water-soluble nanocrystal (NC) sample in PBS. The fluorescein was excited at 476 nm, and the NC at 355 nm. Excitation spectra were collected with detection at 550 nm (fluorescein) and 533 nm (NC) because of the difference in emission spectra. The nanocrystals have a much narrower emission (32 nm compared with 45 nm at half maximum and 67 nm compared with 100 nm at 10% maximum), no red tail, and a broad, continuous excitation spectrum.

Metallic and magnetic nanocrystals, with the appropriate organic derivatization of the surface, have been used widely in biological experiments (*6–11*). The use of semiconductor nanocrystals in a biological context is potentially more problematic because the high surface area of the nanocrystal might lead to reduced luminescence efficiency and photochemical degradation. Bandgap engineering concepts borrowed from materials science and electronics have led to the development of core-shell nanocrystal samples with high, room temperature quantum yields (>50%) (*12–14*) and much improved photochemical stability. By enclosing a core nanocrystal of one material with a shell of another having a larger bandgap, one can efficiently confine the excitation to the core, eliminating nonradiative relaxation pathways and preventing photochemical degradation. The synthesis of the semiconductor nanocrystals and the growth of the shell by methods from the literature yield gram quantities of a variety of materials with a narrow size distribution (5%), coated with a surfactant but soluble only in nonpolar solvents (*15, 16*).

Biological applications require water-soluble nanocrystals. We have extended the chemistry of the core-shell systems by adding a third layer of silica that makes the core-shell water soluble, similar to a procedure detailed for coating gold and cadmium sulfide nanocrystals (*17, 18*). This strategy has a number of advantages compared with strategies that use a single direct bond to the surface of the nanocrystal: the multivalency of an extensively polymerized polysilane ensures that the nanocrystals stay soluble in spite of the potential loss of bound thiol. Furthermore, the chemistry of silica is well characterized and widely used to functionalize supports for chromatography. Modification of the silica surface with different groups can be used to control the interactions with the biological sample. The core-shell nanocrystals prepared in this manner are soluble and stable in water or buffered solution, and they retain a fairly large quantum yield [up to 21%, comparable to some conventionally used fluorescent dyes that have yields between 14 and 71% (*3*)] (Fig. 2B). Further developments in the bandgap engineering of nanocrystals and modifications to the silanization chemistry are expected to result in higher quantum yields and improvement of other emission properties (*19*). This chemistry has been applied to a number of different sized core-shell nanocrystals, generating a spectrally tuned family of probes, all of which are amenable to the same modification chemistry (in contrast to organic dyes, for which specific chemistries must be developed on a case by case basis).

To establish the utility of nanocrystals for biological staining, we fluorescently labeled 3T3 mouse fibroblast cells using two different size CdSe-CdS core-shell nanocrystals enclosed in a silica shell (*20*). The smaller nanocrystals (2-nm core) emitted green fluorescence (maximum 550 nm, 15% quantum yield), the larger (4-nm core), red fluorescence (maximum 630 nm, 6% quantum yield). The surface of the nanocrystals may be tailored to interact with the biological sample either through electrostatic and hydrogen-bonding interactions or through a specific ligand-receptor interaction, such as the avidin-biotin interaction (*21*). As an example of the former, nanocrystals coated with trimethoxysilylpropyl urea and acetate groups were found to bind with high affinity in the cell nucleus. This nuclear binding could be suppressed with an anionic silane reagent [3-(trihydroxysilyl)propyl methylphosphonate] or by incubating with the nanocrystals in a 0.2% SDS solution. This property was used to "stain" the nucleus with the green-colored nanocrystals, relying on the silanized nanocrystal surface to control the binding.

The avidin-biotin interaction, a model

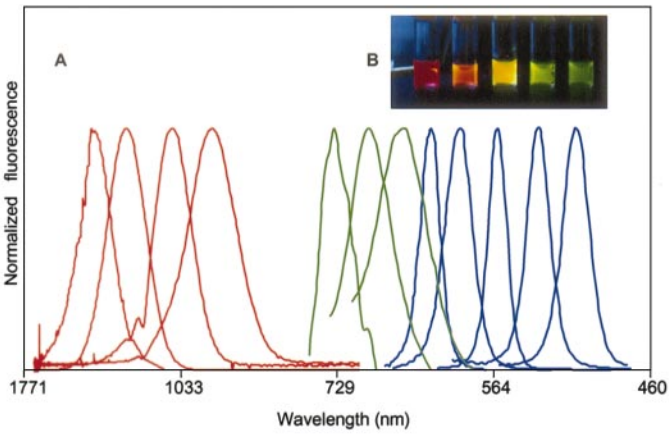

Fig. 2. (**A**) Size- and material-dependent emission spectra of several surfactant-coated semiconductor nanocrystals in a variety of sizes. The blue series represents different sizes of CdSe nanocrystals (*16*) with diameters of 2.1, 2.4, 3.1, 3.6, and 4.6 nm (from right to left). The green series is of InP nanocrystals (*26*) with diameters of 3.0, 3.5, and 4.6 nm. The red series is of InAs nanocrystals (*16*) with diameters of 2.8, 3.6, 4.6, and 6.0 nm. (**B**) A true-color image of a series of silica-coated core (CdSe)–shell (ZnS or CdS) nanocrystal probes in aqueous buffer, all illuminated simultaneously with a handheld ultraviolet lamp.

system for ligand-receptor binding, was used here to specifically label the F-actin filaments with red nanocrystal probes. Biotin was covalently bound to the nanocrystal surface (*22*), and the biotinylated nanocrystals were used to label fibroblasts, which had been incubated in phalloidin-biotin and streptavidin. One round of amplification was carried out by incubating the sample with streptavidin and then with red biotinylated nanocrystals once again.

The resulting samples were imaged with both conventional wide-field and laser-scanning confocal fluorescence microscopes. In contrast to conventional multicolor dye imaging, light from a mercury lamp with a fluorescein isothiocyanate excitation filter and a single long-pass detection filter (515 nm) were used with the wide-field microscope to see both colors at one time. The green and red labels were clearly spectrally resolved to the eye and to a color Polaroid camera. Nonspecific labeling of the nuclear membrane by both the red and the green probes resulted in a yellow color. The red actin filaments, however, were specifically stained. These filaments were not visible or were only very faintly visible in the control experiments lacking phalloidin-biotin. The penetration of the green probes into the nucleus and specific red staining of the actin fibers is readily visible in Fig. 3. Over repeated scans, the nanocrystal-labeled samples showed very little photobleaching, far less than with conventional dye molecules (Fig. 4).

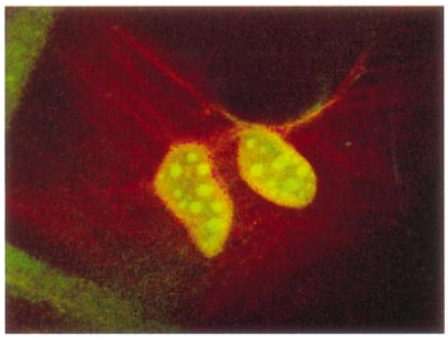

Fig. 3. Cross section of a dual-labeled sample examined with a Bio-Rad 1024 MRC laser-scanning confocal microscope with a 40× oil 1.3 numerical aperture objective. The mouse 3T3 fibroblasts were grown and prepared as described in (*27*). A false-colored image was obtained with 363-nm excitation, with simultaneous two-channel detection (522DF 35-nm FWHM narrow-pass filter for the green, and a 585-nm long-pass filter for the red). Image width: 84 μm.

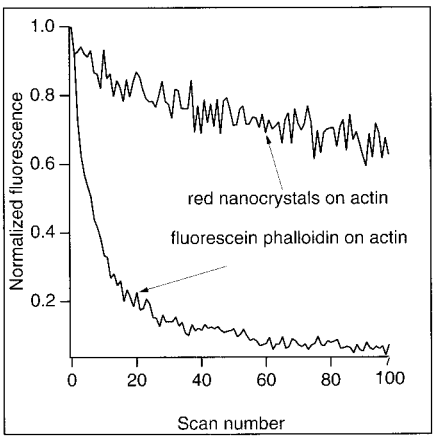

Fig. 4. Sequential scan photostability comparison of fluorescein-phalloidin–labeled actin fibers compared with nanocrystal-labeled actin fibers. Fluorescein was excited at 488 nm and the nanocrystals at 363 nm by a laser scanning confocal microscope with a 12-μs dwell time and ~20-mW power for each laser. The average intensity of four pixels was followed in each sample through 100 successive scans and normalized to its initial value. The intensity of the fluorescein drops quickly to autofluorescence levels, whereas the intensity of the nanocrystals drops only slightly.

The development of nanocrystals for biological labeling opens up new possibilities for many multicolor experiments and diagnostics. Further, it establishes a class of fluorescent probe for which no small organic molecule equivalent exists. The tunability of the optical features allows for their use as direct probes or as sensitizers for traditional probes. These nanocrystals also have a long fluorescence lifetime (hundreds of nanoseconds) (*23*), which can allow for time-gated detection for autofluorescence suppression (*24*). Further developments such as direct immunolabeling, in situ hybridization, and incorporation into microspheres will be important for applications such as cytometry and immunocytobiology. In addition, nanocrystal probes may prove useful for other contrast mechanisms such as x-ray fluorescence, x-ray absorption, electron microscopy, and scintillation proximity imaging, and the use of far red– or infrared-emitting nanocrystals (InP and InAs) as tunable, robust infrared dyes is another possibility.

References and Notes

1. M. Roederer *et al*., *Cytometry* **29**, 328 (1997).
2. E. Schröck *et al*., *Science* **273**, 494 (1996).
3. A. Waggoner, *Methods Enzymol*. **246**, 362 (1995).
4. Attempts with energy transfer–sensitized probes and phycobiliprotein-conjugated dye molecules have been somewhat successful, but the efficiency of energy transfer is lower than the intrinsic excitation and emission of a dye molecule [J. Y. Ju, C. C. Ruan, C. W. Fuller, A. N. Glazer, R. A. Mathies, *Proc. Natl. Acad. Sci. U.S.A.* **92**, 4347 (1995); M. Roederer, A. B. Kantor, D. R. Parks, L. A. Herzenberg, *Cytometry* **24**, 191 (1996)].
5. A. P. Alivisatos, *J. Phys. Chem*. **100**, 13226 (1996).
6. S. Miltenyi, W. Muller, W. Weichel, A. Radbruch, *Cytometry* **11**, 231 (1990).
7. P. M. Lackie, *Histochem. Cell Biol*. **106**, 9 (1996).
8. R. Hermann, P. Walther, M. Muller, *ibid*., p. 31.
9. R. Elghanian, J. J. Storhoff, R. C. Mucic, R. L. Letsinger, C. A. Mirkin, *Science* **277**, 1078 (1997).
10. The idea of using biological interactions to pattern materials has also been explored [A. P. Alivisatos *et al*., *Nature* **382**, 609 (1996); C. A. Mirkin, R. L. Letsinger, R. C. Mucic, J. J. Storhoff, *ibid*., p. 607].
11. H. B. Beverloo, A. van Schadewijk, S. van Gelderen-Boele, H. J. Tanke, *Cytometry* **11**, 784 (1990).
12. A. Eychmuller, A. Mews, H. Weller, *Chem. Phys. Lett*. **208**, 59 (1993).
13. M. A. Hines and P. Guyot-Sionnest, *J. Phys. Chem*. **100**, 468 (1996).
14. X. G. Peng, M. C. Schlamp, A. V. Kadavanich, A. P. Alivisatos, *J. Am. Chem. Soc*. **119**, 7019 (1997).
15. C. B. Murray, D. J. Norris, M. G. Bawendi, *ibid*. **115**, 8706 (1993).
16. X. G. Peng, J. Wickham, A. P. Alivisatos, *ibid*. **120**, 5343 (1998).
17. L. M. Lizmarzan, M. Giersig, P. Mulvaney, *Langmuir* **12**, 4329 (1996).
18. M. A. CorreaDuarte, M. Giersig, L. M. LizMarzan, *Chem. Phys. Lett*. **286**, 497 (1998).
19. M. Nirmal *et al*., *Nature* **383**, 802 (1996).
20. For the synthesis of water-soluble core-shell nanocrystals, 2 to 10 mg of CdSe-CdS (*13*) and CdSe-ZnS (*25*) core-shell nanocrystals were homogeneously dispersed in 2 ml of degassed *n*-butanol then precipitated with anhydrous methanol; addition of a roughly equal mass of trioctylphosphineoxide and 1 hour of heating at 100°C were necessary to disperse the CdSe-CdS. The precipitate was dissolved in 120 ml of a solution of 0.17% (v/v) (3-mercaptopropyl)trimethoxysilane in 25% dimethyl sulfoxide (DMSO) in methanol, the pH of which was adjusted to 10 to 11 with $(CH_3)_4NOH \cdot 5H_2O$. After overnight stirring, the solution was diluted with 100 ml of methanolic $(CH_3)_4NOH \cdot 5H_2O$, at pH 10 and gently refluxed at 69°C for 25 to 30 min. After the preparation was cooled, 200 ml of a 10% water and methanol solution containing 400 μl of trimethoxysilyl propyl urea and 40 μl of 3-aminopropyltrimethoxysilane was added, stirred for 2 hours, then heated to reflux at 69°C for less than 5 min and cooled. Next, 40 ml of a 10% chlorotrimethylsilane solution, basified with $(CH_3)_4NOH \cdot 5H_2O$, was added, the preparation stirred for another 2 hours, then concentrated partially at 60°C in vacuo to an oily solution. This solution was precipitated to a greasy solid with 50% acetone in isopropanol. This solid was redissolved in water and buffered solution.
21. M. Wilchek and E. A. Bayer, *Trends Biochem. Sci*. **14**, 408 (1989).
22. For conversion of functional groups on the surface of the nanocrystals, the precipitated sample was dissolved in 100 mM phosphate-buffered saline (PBS), pH 7.5, at a concentration four times that of the final oily solution. A 1.0-ml volume of the concentrated nanocrystal solution was incubated with 100 to 400 μl of a 10-mg/ml solution of biotinamidocaproic acid 3-sulfo-*N*-hydroxysuccinimide ester (Sigma) in 6% DMSO in PBS for 1 hour, after which the solution was quenched with a neutralized iodoacetic acid solution in PBS to 50 mM final iodoacetate concentration. The unbiotinylated nanocrystals were prepared by adding the quench solution directly. These solutions were incubated overnight at 4°C, then concentrated and rinsed through a Centricon 50 (Millipore) and diluted to 1.0 ml; the remaining amines on the biotinylated nanocrystals were capped with 50 μl of a 1 M solution of succinic anhydride in dry DMSO, followed by addition of an equivalent amount of base and further purification through a Centricon 50. The retentate was diluted to 1.0 ml and used for labeling at 1:10 dilution. The biotinylated nanocrystals shifted to lower mobility in a gel when incubated with streptavidin. Higher levels of biotinylation followed by streptavidin incubation resulted in a further decrease in mobility through agarose gel. These effects were not seen in unbiotinylated nanocrystal samples, indicating that this interaction is specific and that the biotin is covalently bound to the nanocrystal surface.
23. The emission from the nanocrystals is due to a transition that would be spin forbidden in a system of light atoms. Because of strong spin-orbit coupling and quantum confinement effects, the emission has a radiative rate that is on the order of $10^7\ s^{-1}$. In this report, we refer to this emission as the nanocrystal fluorescence [M. Nirmal *et al*., *Phys. Rev. Lett*. **75**, 3728 (1995)].
24. L. Seveus *et al*., *Cytometry* **13**, 329 (1992).
25. B. O. Dabbousi *et al*., *J. Phys. Chem. B* **101**, 9463 (1997).
26. A. A. Guzelian *et al*., *ibid*. **100**, 7212 (1996).
27. Mouse 3T3 fibroblasts were grown on fibronectin-treated, formvar-coated gold grids and fixed with 4% paraformaldehyde, 0.1% glutaraldehyde, and 0.5% Triton at room temperature. Specimens were then treated successively with unbiotinylated green nanocrystals, phalloidin-biotin (Molecular Probes) (15 min), streptavidin (25 μg/ml) (30

min), a ~100 nM solution of biotinylated red nanocrystals (30 min), again streptavidin (30 min), then once more with the red biotinylated nanocrystals (30 min). At least three PBS or Superblock-PBS (Pierce) rinse steps (5 min each) were performed between each incubation. Samples were mounted on microscope slides in PBS.

28. We would like to thank X. Peng, J. Gray, C. Bertozzi, and P. Schultz for many helpful discussions. The photoluminescence spectra of InAs nanocrystals, InP nanocrystals, and CdSe nanocrystals in Fig. 2 were provided by J. Wickham, U. Banin, and X. Peng. Supported by the Director, Office of Energy Research, Office of Basic Energy Sciences, Division of Materials Sciences, of the U.S. Department of Energy under contract number DE-AC03-76SF00098. M.B. acknowledges support from a NSF graduate research fellowship.

27 May 1998; accepted 20 August 1998

Quantum Dot Bioconjugates for Ultrasensitive Nonisotopic Detection

Warren C. W. Chan and Shuming Nie*

Highly luminescent semiconductor quantum dots (zinc sulfide–capped cadmium selenide) have been covalently coupled to biomolecules for use in ultrasensitive biological detection. In comparison with organic dyes such as rhodamine, this class of luminescent labels is 20 times as bright, 100 times as stable against photobleaching, and one-third as wide in spectral linewidth. These nanometer-sized conjugates are water-soluble and biocompatible. Quantum dots that were labeled with the protein transferrin underwent receptor-mediated endocytosis in cultured HeLa cells, and those dots that were labeled with immunomolecules recognized specific antibodies or antigens.

The development of sensitive nonisotopic detection systems has substantially impacted many research areas, such as DNA sequencing, clinical diagnostics, and fundamental molecular biology (*1*). These systems aim to solve the problems of radioactive detection (for example, health hazards and short lifetimes) and open new possibilities in ultrasensitive and automated biological assays. Current nonisotopic detection methods are mainly based on organic reporter molecules that undergo enzyme-linked color changes or that are fluorescent, luminescent, or electroactive (*1*). We have developed a class of nonisotopic detection labels by coupling luminescent semiconductor quantum dots (QDs) to biological molecules. In this design, nanometer-sized QDs are detected through photoluminescence, and the attached biomolecules recognize specific analytes, such as proteins, DNA, or viruses. These nanoconjugates are biocompatible and are suitable for use in cell biology and immunoassay. At the present level of development, however, the QDs are not sufficiently monodisperse, and intermittent photon emission could cause statistical problems at the single-dot level.

Molecular conjugates of luminescent QDs are expected to offer substantial advantages over organic dyes. The properties of QDs result from quantum-size confinement, which occurs when metal and semiconductor particles are smaller than their exciton Bohr radii (about 1 to 5 nm) (*2–4*). Recent advances have resulted in the large-scale preparation of relatively monodisperse QDs (*5–7*), the characterization of their lattice structures (*4*), and the fabrication of QD arrays (*8–12*) and light-emitting diodes (*13*, *14*). For example, CdSe QDs passivated with a ZnS layer are strongly luminescent (35 to 50% quantum yield) at room temperature, and their emission wavelength can be tuned from the blue to the red wavelengths by changing the particle size (*7*, *15*). However, these luminescent QDs are prepared in organic solvents and are not suitable for biological application. Additionally, it is unclear how to attach biomolecules to a QD and still maintain their activity.

We have solved these problems by using mercaptoacetic acid for solubilization and covalent protein attachment. When reacted with ZnS-capped CdSe QDs in chloroform, the mercaptoacetic acid was extracted. Excess mercaptoacetic acid was removed by four or more rounds of centrifugation. The purified QDs were conjugated to transferrin and IgG with the cross-linking reagent ethyl-3-(dimethylaminopropyl)carbodiimide. Standard protocols were followed (*16*), except the excess proteins were removed by repeated centrifugation. The purified conjugates were stored in PBS at room temperature.

Department of Chemistry, Indiana University, Bloomington, IN 47405, USA.

*To whom correspondence should be addressed. E-mail: nie@indiana.edu

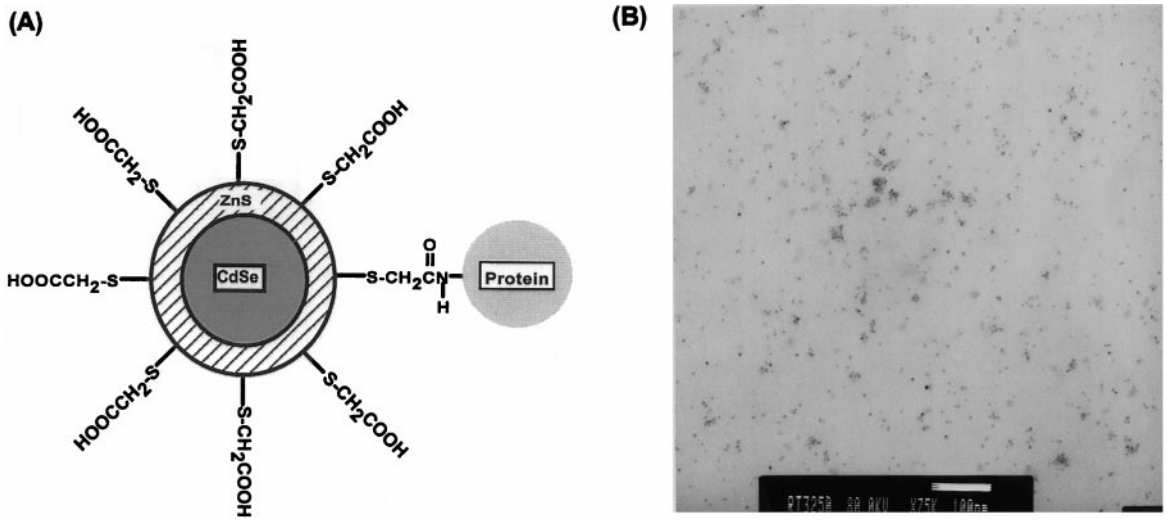

Fig. 1. (**A**) Schematic of a ZnS-capped CdSe QD that is covalently coupled to a protein by mercaptoacetic acid. (**B**) TEM of QD-transferrin (an iron-transport protein) conjugates. Scale bar, 100 nm. Clusters of closely spaced particles were mainly formed by sample spreading and drying on the carbon grid and not by chemical cross-linking. ZnS-capped QDs with a CdSe core size of 4.2 nm were prepared according to the procedure developed by Hines and Guyot-Sionnest (*7*). The colloidal QDs were dissolved in chloroform and were reacted with glacial mercaptoacetic acid (~1.0 M) for 2 hours. An aqueous phosphate-buffered saline (PBS) solution (pH 7.4) was added to this reaction mixture at a 1:1 volume ratio. After vigorous shaking and mixing, the chloroform and water layers separated spontaneously. The aqueous layer, which contained mercapto-coated

capto group binds to a Zn atom, and the polar carboxylic acid group renders the QDs water-soluble (Fig. 1A). The free carboxyl group is also available for covalent coupling to various biomolecules (such as proteins, peptides, and nucleic acids) by cross-linking to reactive amine groups (*16*). In addition, this mercaptoacetic acid layer is expected to reduce passive protein adsorption on QDs. Transmission electron microscopy (TEM) (Fig. 1B) showed that the solubilization and cross-linking steps did not result in aggregation and that the QD bioconjugates were primarily single particles. This finding was also supported by ultrasensitive optical measurements at the single-dot level. A comparison of color luminescence images that were obtained from the original QDs, the water-soluble QDs, and the protein-conjugated QDs (Fig. 2) indicated that the optical properties of QDs remain unchanged after solubilization and conjugation. Bulk optical measurements (*17*) also showed that the emission spectra and efficiencies were similar for the original sample (in chloroform) and the water-soluble QDs. The numbers of mercaptoacetic acid and protein molecules per QD have not been determined experimentally. For steric reasons, perhaps only two to five molecules of a 100-kD protein can be attached to a 5-nm QD, which is similar to the number of protein molecules that can be attached to a 5-nm colloidal gold particle (*16*).

Several lines of evidence suggest that the observed luminescence signals resulted from spatially isolated single QDs. First, the measured particle density was consistent with the value that was calculated from the sample volume and concentration. Second, the colloidal QDs were not homogeneous in size (~5% variation), and the bulk sample showed a single broad emission peak (*7*, *15*). However, when individual QDs were examined, discrete luminescence peaks were observed [as seen in a rainbow of luminescence colors (Fig. 2)]. Third, the discrete luminescence signals showed an intermittent on and off behavior, which was similar to the behavior reported for single fluorescent molecules (*16*, *18*–*20*) and single CdSe QDs (*21*, *22*). This "blinking" behavior may seem fascinating from a fundamental point of view but can cause signal intensity fluctuations in ultrasensitive detection. This problem could be overcome by coating QDs with a thicker ZnS layer and by reducing the excitation light intensity (*21*).

We further compared the photophysical properties of the QD conjugates with those of common organic dyes. Wavelength-resolved spectra and time-resolved photobleaching data, which were obtained from single QDs as well as bulk materials, are shown in Fig. 3. The intrinsic QD spectral width [full width at half maximum (FWHM) is 12 nm] is about one-third as wide as that of a fluorescent sphere (FWHM is 35 nm). Furthermore, the QD emission (time constant $t_{1/2}$ = 960 s) is nearly 100 times as stable as rhodamine 6G (R6G) ($t_{1/2}$ = 10 s) against photobleaching. In this approximate comparison of photobleaching rates, the differences between QD and R6G fluorescence quantum yields were not taken into account. Using wavelength-matched fluorescent latex spheres as a standard, we estimated that the fluorescence intensity of a single CdSe QD is equivalent to that of ~20 rhodamine molecules (*23*). This result compares well with that for the fluorescent protein phycoerythrin, which has a fluorescence intensity equivalent to that of 25 R6G molecules but is unstable photochemically (*24*). However, for the QD bioconjugates to be broadly useful in ultrasensitive analysis, the attached biomolecules must be active and must be able to recognize specific analytes in a complex mixture.

With covalently attached proteins, we demonstrated that the QDs were biocompatible in vitro and with living cells. Fluorescence images obtained from cultured HeLa cells that had been incubated with mercapto-QDs (control) and with transferrin-QD bioconjugates are

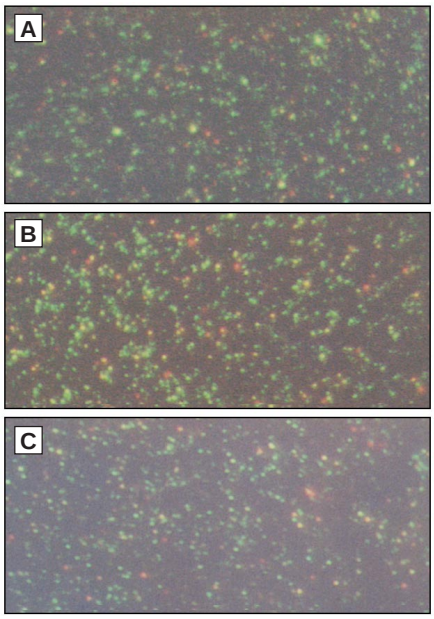

Fig. 2. Color luminescence images obtained from (**A**) original QDs, (**B**) mercapto-solubilized QDs, and (**C**) QD-IgG conjugates. The images were directly recorded on color photographic film (ASA-1600) with a 15-s exposure by a 35-mm camera that was attached to a Nikon inverted optical microscope. Samples of dilute QDs were deposited and spread on polylysine-coated glass coverslips, resulting in spatially isolated single QDs on the surface. Continuous-wave excitation at 514.5 nm was provided by an Ar ion laser (Lexel Laser, Fremont, California). A longpass dielectric filter (Chroma Tech, Brattleboro, Vermont) was used to reject the scattered laser light and to pass the Stokes-shifted luminescent photons. A high-numerical-aperture (NA) (1.3), oil-immersion objective was used, and the total laser power at the sample was 50 mW. There are emission color differences among single QDs.

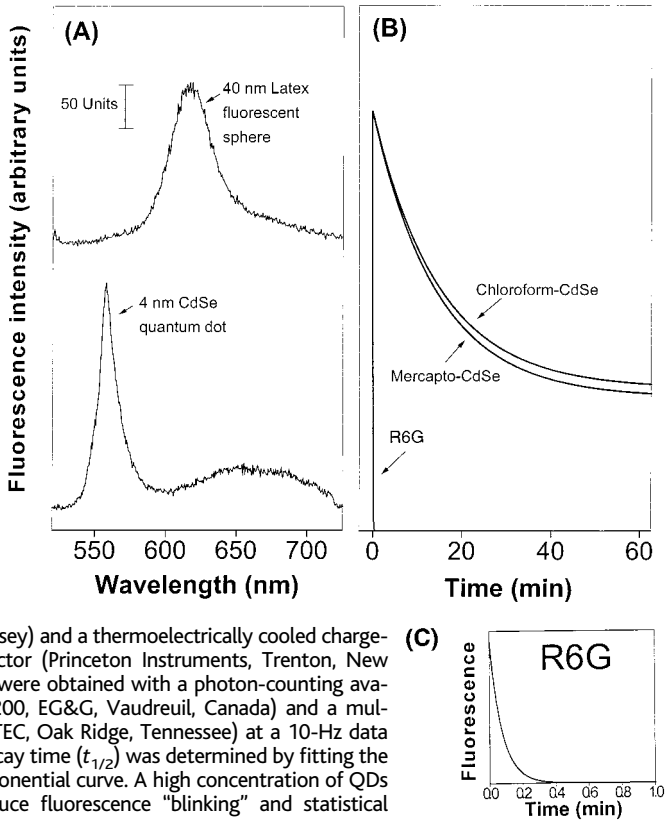

Fig. 3. Comparison of the photophysical properties of luminescent QDs and organic dyes. (**A**) Wavelength-resolved spectra obtained from a single 40-nm fluorescent latex sphere and a single mercapto-QD. The broad emission peak at ~660 nm is believed to result from surface defects on the QD. (**B**) Time-resolved photobleaching curves for the original QDs, the solubilized QDs, and the dye R6G. (**C**) The time-resolved photobleaching curve for R6G is shown in detail. Single-particle spectroscopy was performed with a confocal fluorescence microscope that was attached to a single-stage spectrograph (Model 270M, Spex, Edison, New Jersey) and a thermoelectrically cooled charge-coupled device (CCD) detector (Princeton Instruments, Trenton, New Jersey). Time-resolved data were obtained with a photon-counting avalanche photodiode (SPCM-200, EG&G, Vaudreuil, Canada) and a multichannel scalar (EG&G ORTEC, Oak Ridge, Tennessee) at a 10-Hz data acquisition rate. The half-decay time ($t_{1/2}$) was determined by fitting the experimental data to an exponential curve. A high concentration of QDs and R6G was used to reduce fluorescence "blinking" and statistical fluctuation.

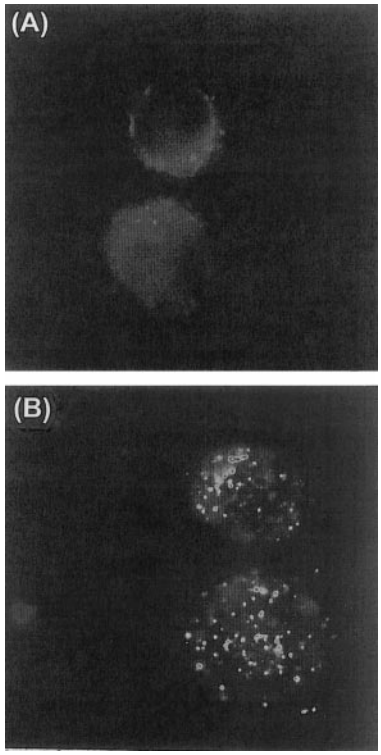

Fig. 4. Luminescence images of cultured HeLa cells that were incubated with (**A**) mercapto-QDs and (**B**) QD-transferrin conjugates. The QD bioconjugates were transported into the cell by receptor-mediated endocytosis and were detected as clusters or aggregates. Luminescence "blinking" was not observed for these clusters because of statistical averaging. The images were obtained with an epifluorescence microscope that was equipped with a high-resolution CCD camera (1.4 million pixels) (Photometrix, Tucson, Arizona) and a 100-W Hg excitation lamp. HeLa cells were grown in a minimum essential medium containing 10% fetal calf serum, 1% antibiotics (penicillin and streptomycin), and fungizone. The cultured cells were incubated overnight with either control QDs or the transferrin conjugates at 37°C. After repeated washings to eliminate excess QDs, the cells were removed from the petri dish and placed on a glass cover slip for imaging. The trypsin-treated cells had a spherical shape on the cover slip. Cell diameter, ~10 μm.

shown in Fig. 4. In the absence of transferrin, no QDs were observed inside the cell, and the image resulted from weak cellular autofluorescence. When transferrin was present, receptor-mediated endocytosis occurred, and the luminescent QDs were transported into the cell (*25*). Clearly, the attached transferrin molecules were still active and were recognized by the receptors on the cell surface. As with nanometer-sized colloidal gold, the QD labels did not substantially interfere with ligand-receptor binding or endocytosis.

We also investigated the suitability of QD labels for sensitive immunoassay. The fluorescence images of QD–immunoglobulin G (IgG) conjugates that were incubated with

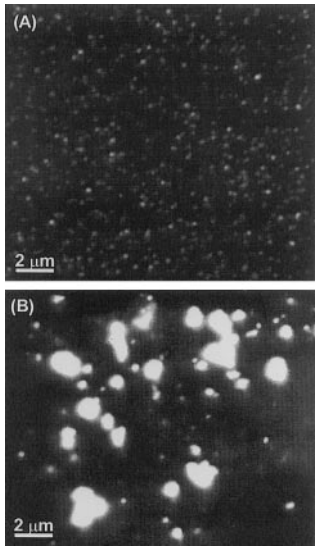

Fig. 5. Antibody-induced agglutination of QDs that were labeled with human IgG. (**A**) Luminescence image of QD conjugates in the presence of BSA (0.5 mg/ml). (**B**) Luminescence image of aggregated QDs induced by a specific polyclonal antibody (0.5 μg/ml).

bovine serum albumin (BSA) (0.5 mg/ml) and with a specific polyclonal antibody (0.5 μg/ml) are shown in Fig. 5. The polyclonal antibody recognized the Fab fragments of the immunoglobulin and led to extensive aggregation of the QDs. In contrast, well-dispersed and primarily single QDs were detected in the presence of BSA (*26*). This simple experiment showed that the attached immunomolecules can recognize specific antibodies or antigens. The observed aggregation of QDs was similar to latex immunoagglutination, which is a technique that is widely used in clinical diagnostics (*27*).

In conclusion, semiconductor QDs have been covalently attached to biomolecules for ultrasensitive detection at the single-dot level. We envision that the improved photostability could allow real-time observations of ligand-receptor interaction and of molecular trafficking in living cells. Also, current combinatorial labeling with traditional organic dyes allows only 25 DNA sequences to be detected simultaneously (*28*). Further synthetic efforts may produce sufficiently monodispersed QDs (*29*), which should be important toward developing multiplexed detection schemes. When combined with sandwich immunoassay or nucleic acid hybridization, the use of QD probes should open new possibilities in detecting single native biomolecules, such as cytokines and viral RNA.

References and Notes

1. For recent books, see L. J. Kricka, Ed., *Nonisotopic Probing, Blotting, and Sequencing* (Academic Press, New York, 1995); P. G. Issac, Ed., *Protocols for Nucleic Acid Analysis by Nonradioactive Probes* (Humana, Totowa, NJ, 1994); E. P. Diamandis and T. K. Christopoulos, Eds., *Immunoassay* (Academic Press, New York, 1996).
2. A. P. Alivisatos, *Science* **271**, 933 (1996); *J. Phys. Chem.* **100**, 13226 (1996).
3. L. E. Brus, *Appl. Phys. A* **53**, 465 (1991); W. L. Wilson, P. F. Szajowski, L. E. Brus, *Science* **262**, 1242 (1993).
4. A. Henglein, *Chem. Rev.* **89**, 1861 (1989); H. Weller, *Angew. Chem. Int. Ed. Engl.* **32**, 41 (1993).
5. C. B. Murray, D. J. Norris, M. G. Bawendi, *J. Am. Chem. Soc.* **115**, 8706 (1993).
6. J. E. Bowen Katari, V. L. Colvin, A. P. Alivisatos, *J. Phys. Chem.* **98**, 4109 (1994).
7. M. A. Hines and P. Guyot-Sionnest, *ibid.* **100**, 468 (1996).
8. C. B. Murray, C. R. Kagan, M. G. Bawendi, *Science* **270**, 1335 (1995).
9. R. P. Andres *et al.*, *ibid.* **273**, 1690 (1996).
10. J. R. Heath *et al.*, *J. Phys. Chem.* **100**, 3144 (1996); C. P. Collier, R. J. Saykally, J. J. Shiang, S. E. Henrichs, J. R. Heath, *Science* **277**, 1978 (1997).
11. C. A. Mirkin, R. L. Letsinger, R. C. Mucic, J. J. Storhoff, *Nature* **382**, 607 (1996).
12. A. P. Alivisatos *et al.*, *ibid.*, p. 609.
13. V. L. Colvin, M. C. Schlamp, A. P. Alivisatos, *ibid.* **370**, 354 (1994).
14. B. O. Dabbousi, M. G. Bawendi, O. Onotsuka, M. F. Rubner, *Appl. Phys. Lett.* **66**, 1316 (1995).
15. B. O. Dabbousi *et al.*, *J. Phys. Chem. B* **101**, 9463 (1997).
16. G. T. Hermanson, *Bioconjugate Techniques* (Academic Press, New York, 1996).
17. W. C. W. Chan and S. Nie, unpublished data.
18. R. M. Dickson, A. B. Cubitt, R. Y. Tsien, W. E. Moerner, *Nature* **388**, 355 (1997).
19. H. P. Lu and X. X. Xie, *ibid.* **385**, 143 (1997).
20. D. A. Vanden *et al.*, *Science* **277**, 1074 (1997).
21. M. Nirmal *et al.*, *Nature* **383**, 802 (1996); S. A. Empedocles, D. J. Norris, M. G. Bawendi, *Phys. Rev. Lett.* **77**, 3873 (1996).
22. S. A. Blanton, M. A. Hines, P. Guyot-Sionnest, *Appl. Phys. Lett.* **69**, 3905 (1996).
23. The 40-nm fluorescent latex spheres (λ_{ex} = 530 nm; λ_{em} = 560 nm) (λ_{ex}, excitation wavelength maximum; λ_{em}, emission wavelength maximum) were purchased from Molecular Probes (Eugene, OR). Each sphere is equivalent in intensity to ~350 dye molecules [R. P. Haugland, *Handbook of Fluorescent Probes and Research Chemicals* (Molecular Probes, Eugene, OR, ed. 6, 1995)]. The integrated emission intensities for single QDs and single latex spheres were measured and compared under identical experimental conditions. The single-dot photoluminescence was about one-seventeenth that of a single latex sphere and thus was estimated to be equal to the total emission intensity of 20 R6G molecules.
24. K. Peck, L. Stryer, A. N. Glazer, R. A. Mathies, *Proc. Natl. Acad. Sci. U.S.A.* **86**, 4087 (1989).
25. D. A. Edwards, K. J. Gooch, I. Zhang, G. H. McKinley, R. Langer, *ibid.* **93**, 1786 (1996); E. Smythe and G. Warren, *Eur. J. Biochem.* **202**, 689 (1991).
26. Quantitative measurements showed that the intensity variations among the discrete luminescent signals were within a factor of 3. Thus, the observed signals arose primarily from single QDs and, perhaps, a small population of double- and triple-dot aggregates. Protein BSA should adsorb nonspecifically on the QDs, but it did not cause particle aggregation.
27. L. B. Bangs, *Pure Appl. Chem.* **68**, 1873 (1996).
28. M. R. Speicher, S. G. Ballard, D. C. Ward, *Nature Genet.* **12**, 368 (1996).
29. X. Peng, J. Wickman, A. P. Alivisatos, *J. Am. Chem. Soc.* **120**, 5343 (1998).
30. We are grateful to M. A. Hines and P. Guyot-Sionnest for their help in QD synthesis and for providing the original ZnS-capped CdSe sample. We also thank A. K. Reuter for bulk optical measurement, R. Turner for TEM, and S. R. Emory for valuable discussions. This work was supported in part by NSF grant CHE-9610254 and by the Petroleum Research Fund grant 32231-AC5. S.N. acknowledges the Whitaker Foundation for a Biomedical Engineering Award and the Beckman Foundation for a Beckman Young Investigator Award.

17 June 1998; accepted 27 August 1998